

## Embryonic zeolites for highly efficient synthesis of dimethyl ether from syngas

Palčić, Ana; Jaén, Sara Navarro; Wu, Dan; Cai, Mengdie; Liu, Chong; Pidko, Evgeny A.; Khodakov, Andrei Y.; Ordonsky, Vitaly; Valtchev, Valentin

**DOI**

[10.1016/j.micromeso.2021.111138](https://doi.org/10.1016/j.micromeso.2021.111138)

**Publication date**

2021

**Document Version**

Final published version

**Published in**

Microporous and Mesoporous Materials

**Citation (APA)**

Palčić, A., Jaén, S. N., Wu, D., Cai, M., Liu, C., Pidko, E. A., Khodakov, A. Y., Ordonsky, V., & Valtchev, V. (2021). Embryonic zeolites for highly efficient synthesis of dimethyl ether from syngas. *Microporous and Mesoporous Materials*, 322, Article 111138. <https://doi.org/10.1016/j.micromeso.2021.111138>

**Important note**

To cite this publication, please use the final published version (if applicable).  
Please check the document version above.

**Copyright**

Other than for strictly personal use, it is not permitted to download, forward or distribute the text or part of it, without the consent of the author(s) and/or copyright holder(s), unless the work is under an open content license such as Creative Commons.

**Takedown policy**

Please contact us and provide details if you believe this document breaches copyrights.  
We will remove access to the work immediately and investigate your claim.



## Embryonic zeolites for highly efficient synthesis of dimethyl ether from syngas

Ana Palčić<sup>a</sup>, Sara Navarro Jaén<sup>b</sup>, Dan Wu<sup>b</sup>, Mengdie Cai<sup>b</sup>, Chong Liu<sup>c</sup>, Evgeny A. Pidko<sup>c</sup>, Andrei Y. Khodakov<sup>b</sup>, Vitaly Ordonsky<sup>b,\*</sup>, Valentin Valtchev<sup>d,\*\*</sup>

<sup>a</sup> Ruđer Bošković Institute, Division of Materials Chemistry, Laboratory for Synthesis of New Materials, Bijenička Cesta 54, Zagreb, Croatia

<sup>b</sup> Univ. Lille, CNRS, Centrale Lille, Univ. Artois, UMR 8181 - UCCS – Unité de Catalyse et Chimie Du Solide, F-59000 Lille, France

<sup>c</sup> Inorganic Systems Engineering, Department of Chemical Engineering, Delft University of Technology, Van der Maasweg 9, 2629 HZ Delft, the Netherlands

<sup>d</sup> Normandie Univ, ENSICAEN, UNICAEN, CNRS, Laboratoire Catalyse et Spectrochimie, 6 Boulevard Maréchal Juin, Caen, France

### ARTICLE INFO

#### Keywords:

Embryonic zeolite  
Acid sites  
DME synthesis  
Syngas

### ABSTRACT

Embryonic X-ray amorphous semi-formed MFI-type zeolite units mixed with the Cu–Zn–Al catalyst have been used for the direct synthesis of dimethyl ether (DME) from syngas. The hybrid catalyst with embryonic zeolite (EZ) with the particle size of 5 nm has demonstrated superior performance in terms of activity, selectivity, and stability compared to the crystalline ZSM-5 zeolite counterpart and the amorphous aluminosilicate material. The FTIR pyridine adsorption uncovered several types of active sites in EZ, including Brønsted acid sites of medium strength. The DFT modeling pointed out the key role of defect sites leading to lower strength of the acid sites in the embryonic MFI zeolite in comparison with the fully crystalline material. The effect of embryonic zeolite on the DME synthesis has been assigned to enhanced transport of methanol from Cu to ultra-small zeolite precursor units with moderate acidity, hence promoting the efficient dehydration to DME with high selectivity and stability.

### 1. Introduction

Zeolites are crystalline microporous materials with the tetrahedron as the essential constituent of their structure. The presence of acid sites at defined positions together with the unique micropore topology governs the usage of zeolites as catalysts that may present reactant, transition state, product, or shape selectivity. However, due to the rigid framework and well-defined size of the pores, the molecule's maximal size that can be processed is close to or smaller than the pore dimensions. Furthermore, in conjunction with the size and morphology of the crystals, mass transport constraints on both, reactants and products, may ensue [1]. The strategies to suppress the diffusion limitation and thus improve catalyst effectiveness and total performance involve reducing the size of the zeolite crystals [2–4] and preparing crystals with larger voids, usually mesopores [5–7] but also extra-large pore zeolites [8]. However, there is still not a zeolitic material with extra-large pores that could face the requirements of chemical and (hydro)thermal stability, chemical reactivity, and affordable production conditions. A new route

was recently presented for overcoming the mass transfer limitations in the zeolites by decreasing their size to the unit cell dimension [9]. These materials are ultra-small (3–5 nm) X-ray amorphous zeolitic units [10]. Their properties and catalytic performance in bulky molecules conversion expand the utilization of already existing crystalline zeolites and offer new opportunities [11]. Recently, a substantial advance in the control of porosity, acidity, and substrate molecules' accessibility of the embryonic zeolites was achieved, which opened the route for new catalytic applications [12]. Namely, materials having extra-large pores (1–2 nm) and acid sites of moderate strength were prepared. These embryonic zeolites are highly active catalysts in the dealkylation of bulky 1,3,5-triisopropylbenzene [11]. Hence, herein is proposed the application of embryonic MFI-type zeolites for designing efficient catalysts for DME synthesis from syngas.

Dimethyl ether (DME) is the simplest ether, and nowadays, it is considered an alternative to conventional fossil diesel fuels [13]. It is an important intermediate for synthesizing different chemicals [14]. Dimethyl ether synthesis can also be regarded as an alternative

\* Corresponding author. Unité de Catalyse et de Chimie du Solide, UMR 8181 CNRS, Ecole Centrale de Lille, Université de Lille Bât. C3, 59655 Villeneuve d'Ascq, France.

\*\* Corresponding author. Normandie Univ, ENSICAEN, UNICAEN, CNRS, Laboratoire Catalyse et Spectrochimie, 6 Boulevard Maréchal Juin, Caen, France.

E-mail addresses: [vitaly.ordonsky@univ-lille.fr](mailto:vitaly.ordonsky@univ-lille.fr) (V. Ordonsky), [valentin.valtchev@ensicaen.fr](mailto:valentin.valtchev@ensicaen.fr) (V. Valtchev).

<https://doi.org/10.1016/j.micromeso.2021.111138>

Received 10 March 2021; Received in revised form 26 April 2021; Accepted 28 April 2021

Available online 4 May 2021

1387-1811/© 2021 Elsevier Inc. All rights reserved.

technology to Fischer-Tropsch transformation of syngas produced from biomass as a renewable resource. The DME is produced in two steps with CO hydrogenation to methanol over a copper-based catalyst and subsequent methanol dehydration to DME over acid catalysts [15]. The methanol yield is low due to the thermodynamic limitation, which makes the product expensive [16]. In the direct DME synthesis from syngas, the thermodynamic equilibrium is shifted to the target product [17,18]. It results in a significant increase in the conversion of CO and higher DME productivities, but the presence of water and CO in the reactor leads to water gas shift reaction:  $\text{CO} + \text{H}_2\text{O} = \text{CO}_2 + \text{H}_2$ .

The direct synthesis of DME requires therefore, bifunctional hybrid catalysts possessing metallic and acidic functions. The most common catalyst for the CO hydrogenation to methanol is Cu–Zn–Al (CZA) containing highly dispersed Cu nanoparticles stabilized by ZnO [19–21]. This material is cheap and can be easily prepared by co-precipitation [17,22]. Acidic catalyst is needed for dehydration of methanol, and the zeolites have been found to be the most appropriate due to their tunable acidity and high hydrothermal stability [23,24]. Traditionally, ZSM-5 has been used for DME synthesis [25], yet other zeolite materials (FER, MCM-22, ITQ, SAPO-5, -11 -21) have also been tested for this reaction [26,27].

There are several issues related to the bifunctional catalyst for DME synthesis. Firstly, the activity of the catalyst depends on the close contact between metal and zeolite active sites. Accordingly, a decrease in the size of zeolite particles in the intimate mixing with CZA leads to a significant increase in the catalytic activity due to the fast transfer of methanol from the metal function to the zeolite [28]. Strong acid sites induce a deeper transformation of methanol and generate hydrocarbons, thus decreasing the selectivity to DME. The catalyst deactivation is another important problem during DME synthesis. It has been attributed to copper oxidation, migration [29] and sintering in the presence of water and acid sites of zeolites [30]. The catalyst deactivation was also associated with the coking [31]. The literature data analysis shows that an optimized catalyst of high activity, selectivity, and stability for DME synthesis has to include close proximity of metal and acid sites of medium strength. These criteria might be fulfilled by the embryonic zeolites, and hence the objective of present study is to evaluate their potential as catalysts for DME synthesis.

## 2. Experimental section

### 2.1. Catalyst preparation

The CuO–ZnO–Al<sub>2</sub>O<sub>3</sub> catalyst (Cu:Zn:Al = 60:30:10 atomic ratio) was prepared by co-precipitation at constant pH (ca. 7) at 70 °C. Aqueous solutions of copper(II) nitrate (0.6 M), zinc nitrate (0.3 M) and aluminum nitrate (0.1 M) were mixed at 70 °C. Afterward, a 0.5 M Na<sub>2</sub>CO<sub>3</sub> solution was added drop by drop. The resulting precipitate was kept under stirring at 70 °C at a constant pH of 7 for 1 h. The precipitate was then filtered, thoroughly washed with distilled water, and dried at 100 °C overnight. The solid was finally calcined at 350 °C for 4 h, at a heating rate of 2 °C·min<sup>-1</sup>.

The embryonic zeolite was synthesized using tetrapropylammonium hydroxide (TPAOH, Alfa Aesar, 1 M), tetraethoxysilane (TEOS, Aldrich, 98%), di-*sec*-butoxyaluminumoxytriethoxysilane (DSBATES, ABCR GMBH), and doubly distilled water produced in our laboratory. Firstly, the needed amount of TPAOH was mixed with the water in a polypropylene bottle, followed by the addition of DSBATES. Upon 24 h stirring, TEOS was added, giving a reaction mixture with the following molar composition 25 DSBATES: 9 TPAOH: 127 TEOS: 500H<sub>2</sub>O. The solution was stirred for an additional 24 h and subsequently treated for 10 days at 100 °C in a convection oven. The recovered solid phase has been washed three times with acetone and then with water until a neutral pH was attained. 3 g of the sample was further three times treated with ammonia chloride solution, (c(NH<sub>4</sub>Cl)=0.5 M, Alfa Aesar, 98%; V(solution) = 30 cm<sup>3</sup>), each time for 4 h at 80 °C. Next, the washed material was calcined

for 10 h at 550 °C, and thus the EZ sample was obtained.

Two types of reference catalysts have been employed to evaluate the catalytic properties of embryonic zeolite. The first reference catalyst is an amorphous aluminosilicate denoted as SiO<sub>2</sub>–Al<sub>2</sub>O<sub>3</sub> with a Si/Al ratio similar to the EZ. The adequate amounts of tetraethyl orthosilicate (Sigma-Aldrich, 98%) and aluminum isopropoxide (Sigma-Aldrich, ≥ 98%) to obtain a Si/Al molar ratio equal to 3 were added to 12 mL of water and 28 mL of ethanol, and the pH was raised to 10 by the addition of ammonia (Merck, 28–30%). The resulting gel was then kept at 25 °C for 24 h, dried at 100 °C overnight, and finally calcined at 500 °C for 6 h at a heating rate of 2 °C·min<sup>-1</sup>. Two zeolites were used as reference catalysts: ZSM-5 with Si/Al ratio of 40, purchased from Süd-Chemie (ZSM-5(40)), and ZSM-5 with Si/Al ratio of 13 purchased from Zeolyst (ZSM-5(13)).

The hybrid catalysts were prepared according to the following procedure: the CZA and zeolite powders were ground in an agate mortar at a mass ratio of 5:3 (w/w) to form a homogeneous hybrid catalyst, followed by pressuring the mixture into tablets and crushing them to 90–150 mesh size particles before the reaction.

### 2.2. Characterization

The powder X-ray diffraction of the samples was measured employing a PANalytical X'Pert Pro diffractometer with Cu K $\alpha$  radiation ( $\lambda = 1.5418 \text{ \AA}$ , 45 kV, 40 mA). The electron micrographs of the prepared crystals were collected by MIRA-LMH (Tescan) SEM equipped with a field emission gun. For TEM analysis, a JEOL-2011F having an acceleration voltage of 200 kV was used. Prior to TEM characterization, the samples were dispersed in ethanol solution with ultrasonic treatment for 30 min and then dropped onto a carbon film on a copper grid.

The elemental analysis of the studied ZSM-5 materials was performed by inductively coupled plasma-atomic emission spectrometer (ICPAES) OPTIMA 4300 DV (Perkin–Elmer). The chemical composition of the samples was analyzed by inductively coupled plasma-atomic emission spectroscopy (ICP-AES) using an OPTIMA 4300 DV (Perkin–Elmer) instrument.

The porosity of the samples was evaluated by recording the nitrogen adsorption/desorption isotherms using a Micrometrics ASAP 2020 volumetric adsorption analyzer. The samples were degassed at 300 °C under a vacuum overnight prior to the measurement. The specific surface area, S<sub>BET</sub>, was calculated by the Brunauer-Emmett-Teller method, and the total pore volume was taken from the nitrogen adsorbed volume at p/p<sub>0</sub> = 0.99. The micropore volume was estimated by the t-plot method, while the mesoporous volume is the difference between the total and micropore volumes, V<sub>meso</sub> = V<sub>total</sub> – V<sub>mic</sub>.

The solid-state MAS NMR spectra were measured on a Bruker Avance III-HD 500 (11.7 T) spectrometer using 4 mm-OD zirconia rotors. Single-pulse excitation (30° flip angle) of 3  $\mu$ s was used for <sup>29</sup>Si MAS NMR experiment and 30 s of recycling delay at a spinning frequency of 12 kHz. <sup>27</sup>Al MAS NMR was performed with a 12 pulse (selective pulse) and a spinning speed of 14.5 kHz.

The IR spectra of as-synthesized porous materials were recorded on a Nicolet Impact 410 FTIR spectrometer equipped with a DTGS detector in the range 400–4000 cm<sup>-1</sup>. The solid materials were pressed into self-supported thin pellets. The pre-treatment in the IR cell connected to the vacuum line at 120 °C (0.33 °C min<sup>-1</sup>) for 1.5 h and at 500 °C (1.27 °C min<sup>-1</sup>) for 2 h under the pressure of 10<sup>-6</sup> torr preceded acquiring the spectra at room temperature. The obtained spectra were normalized to the weight of the self-supported disc. Pyridine adsorption was conducted at 150 °C. After the pressure of 1 torr was established at equilibrium, the cell was evacuated at room temperature. The strength of the interactions between the zeolite and the probe molecules, the samples were step-wise heated to 50–400 °C (step 50 °C), and the spectra were taken at each temperature. After background subtraction, the amount of Brønsted and Lewis acid sites at each desorption temperature was calculated from the integrated area of the bands of

adsorbed pyridine at 1545 and 1455  $\text{cm}^{-1}$  by using the extinction coefficients reported earlier [32].

### 2.3. DFT modeling

Periodic DFT calculations were performed using the Vienna Ab initio Simulation Package (VASP) [33–35]. The Perdew-Burke-Ernzerhof (PBE) exchange-correlation functional in combination with the projector augmented waves (PAW) method was used [36–38]. The kinetic cutoff energy of the plane-wave basis set was set to 500 eV. A Gaussian smearing of 0.05 eV was applied to band occupations around the Fermi level, and the total energies were extrapolated to  $\sigma \rightarrow 0$ . Brillouin zone sampling was restricted to the  $\Gamma$  point [39]. Van der Waals interactions were described by the dispersion-corrected DFT-D3 method with Becke-Johnson (BJ) damping [40]. Convergence was assumed with the force on each atom below 0.05 eV  $\text{\AA}^{-1}$ .

The ZSM-5 zeolite was simulated by an orthogonal MFI unit cell ( $\text{Si}_{96}\text{O}_{192}$ ) [41]. The Brønsted acid sites (BASs) were introduced as charge-compensating cations by the isomorphous substitution of Al for lattice Si atoms. Two MFI models with varying Si/Al ratios of 47 and 3.8 (Figure S1, SI MFI-47 and MFI-3.8) were considered to model the crystalline zeolites. The lattice parameters were optimized for these defect-free zeolite models (MFI-47,  $a = 20.02 \text{ \AA}$ ,  $b = 19.90 \text{ \AA}$ ,  $c = 13.38 \text{ \AA}$ ,  $\alpha = \beta = \gamma = 90^\circ$ ; MFI-3.8,  $a = 20.21 \text{ \AA}$ ,  $b = 19.81 \text{ \AA}$ ,  $c = 13.34 \text{ \AA}$ ,  $\alpha = \beta = \gamma = 90^\circ$ ). To simulate the embryonic MFI zeolite, a  $1 \times 2 \times 2$  supercell was first constructed from the MFI-47 model. Then a part of zeolite framework atoms was removed to build the defect model (Figure S1, SI MFI-defect), in which the BASs (sites 1 and 2) are surrounded by a different portion of the framework atoms as present in the crystalline MFI. The dangling bonds at the edges were saturated by hydrogen atoms. Fully relaxed optimizations were performed with fixed lattice parameters. The BASs at the intersection of MFI channel were considered for the evaluation of acid strength, which was determined by the pyridine adsorption energy ( $\Delta E_{\text{ads}}$ ) computed as

$$\Delta E_{\text{ads}} = E_{\text{model-py}} - E_{\text{model}} - E_{\text{py}}$$

where  $E_{\text{model-py}}$ ,  $E_{\text{model}}$ , and  $E_{\text{py}}$  are the electronic energies of pyridine adsorption complex, free-state pyridine, and bare zeolite model, respectively.

### 2.4. Catalysis

The DME synthesis reaction was carried out in a fixed-bed stainless-steel tubular reactor ( $d = 8 \text{ mm}$ ) operating at 20 bar. The catalyst loading was typically 0.5 g. Before reaction, the samples were reduced in hydrogen flow with a flow rate of 30  $\text{cm}^3/\text{min}$ . During the reduction, the temperature was increased to 290  $^\circ\text{C}$  with a ramping rate of 2  $^\circ\text{C}/\text{min}$  and then kept at this temperature for 7 h. After reduction, the hydrogen flow was switched to a syngas mixture with  $\text{H}_2/\text{CO}$  molar ratio of 2. The reaction was carried out at 260  $^\circ\text{C}$  under a pressure of 20 bar maintained using a back pressure regulator, and the space velocity of 3.6  $\text{L}/\text{g h}$  ( $\text{WHSV} = 1.7 \text{ h}^{-1}$ ). Carbon monoxide contained 5% nitrogen, which was used as an internal standard for conversion and selectivity calculations. The products were sampled from the high-pressure side and analyzed using an online gas chromatograph with a TCD ( $\text{N}_2$ ,  $\text{CO}$ ,  $\text{CO}_2$ , and  $\text{CH}_4$ ) and a FID (MeOH, DME, and hydrocarbons) detectors.

The CO conversion ( $X$ ) was calculated based on the molar flow rate of CO in the feed ( $F_{\text{COin}}$ ) and in the outlet streams ( $F_{\text{COout}}$ ):  $X_{\text{CO}}(\%) = (1 - (F_{\text{COout}}/F_{\text{COin}})) \times 100$ .

The selectivity to the product  $p$  with flow rate  $n_p$  containing  $C_p$  carbon atoms was determined on a carbon basis and expressed in mol % of carbon converted to a specific reaction product:

$$S \text{ to the product } p(\%) = n_p \times C_p / (F_{\text{COin}} - F_{\text{COout}}) \times 100$$

## 3. Results and discussion

### 3.1. Preparation of embryonic zeolite

The embryonic zeolite used in the study was prepared using TPAOH, a structure-directing agent typical for the synthesis of MFI-type zeolite materials. In contrast to previous studies [12–14], where EZs with relatively high Si/Al (>50) ratio were prepared, the Si/Al ratio was kept low. A particular Si and Al source where the bond Si–O–Al already exists, di-*sec*-butoxyaluminumoxytriethoxysilane (DSBATES), was employed. An additional Si source, tetraethylorthosilicate (TEOS) was also employed and enabled achieving Si/Al ratio of 5 in the initial synthesis mixture. Thus, the initial mixture contained a higher Al amount than TPA-templated ZSM-5 can integrate into the zeolite framework. Consequently, aluminum species of different coordination and acid strength can be expected. The solid recovered after 10 days of hydrothermal treatment was further treated with  $\text{NH}_4\text{Cl}$  solution prior to calcination to remove the soluble aluminosilicates deposited on the zeolite precursor and non-reacted TPA cations.

Scanning electron microscopy (SEM) has been used to investigate zeolite morphology. Representative SEM micrographs of zeolite samples are displayed in Fig. 1. The commercial zeolite ZSM-5(40) (Fig. 1A) contains rather small aggregates with a size of about 0.5  $\mu\text{m}$ . These aggregates are built of smaller zeolite nanoparticles (20–50 nm). ZSM-5 (13) (Fig. 1B) is composed of several micron large aggregates built of well-shaped 100–500 nm zeolite crystals with sharper edges. The TEM inspection of the EZ sample showed ultra-small (ca.5 nm) particles, which are loosely agglomerated (Fig. 1C and D). They do not exhibit specific morphological features and, at a closer look, seem to be built up of even smaller entities Fig. 1D.

The physicochemical characteristics of the EZ and conventional zeolites are summarized in Table 1. The EZ material with a bulk Si/Al ratio of 4.83 is X-ray amorphous compared to the completely crystalline reference ZSM-5 samples (Fig. 2A). The Si/Al ratio in EZ is close to the Si/Al ratio in the synthesis mixture (Si/Al = 5), which indicates on the fact that the Si/Al ratio of embryonic zeolites can be controlled by the composition of the initial mixture. The two ZSM-5 materials exhibit the typical of zeolite-type microporous materials type I adsorption isotherm with a steep uptake at low relative pressure. Besides, a second uptake at higher relative pressure originating from the textural mesopores generated by the zeolite nanocrystals can be observed for the ZSM-5(40) material. The EZ material exhibits a type Ib  $\text{N}_2$  adsorption isotherm (Fig. 2B), which ensues from extra-large micropores [42]. The isotherm does not exhibit additional features revealing the high uniformity of the material. The micropore volume of EZ is 0.11  $\text{cm}^3 \text{ g}^{-1}$  and  $S_{\text{BET}}$  = of 363  $\text{m}^2 \text{ g}^{-1}$ , which are lower than for the crystalline materials (Table 1), The amorphous aluminosilicate ( $\text{SiO}_2\text{-Al}_2\text{O}_3$ ) prepared as a reference material has relatively low surface area and microporous volume (Table 1).

The  $^{27}\text{Al}$  MAS NMR analysis found a range of Al species in the studied embryonic zeolite, whereas the crystalline ZSM-5 samples exhibit only a resonance at 54 ppm corresponding to tetrahedral framework Al (Fig. 2C). Further, the IR spectrum of the EZ material displays exclusively isolated silanols (3720–3750  $\text{cm}^{-1}$ ) that were observed in the ZSM-5(40) and ZSM-5(13). Yet crystalline zeolite samples show different band profiles (Fig. 2). Moreover, the crystalline MFI-type material possesses Brønsted acid sites, as evidenced by a well-expressed 3612  $\text{cm}^{-1}$  band. The IR data on the ZSM-5(40) and the ZSM-5(13) samples reveal the presence of highly distorted tetrahedral Al species partially detached from the zeolite framework (3666  $\text{cm}^{-1}$ ) and octahedral extra-framework Al (3880  $\text{cm}^{-1}$ ) [43]. Indeed, there are structural defects in the reference samples, yet  $^{27}\text{Al}$  NMR was not able to detect them, which can be explained by their low fraction combined with the “invisible aluminum” effect.

To evaluate the acid site density, the pyridine probe was adsorbed on the samples and monitored by IR spectroscopy (Table 1 and Table S1, SI). The embryonic and crystalline materials possess both Brønsted and

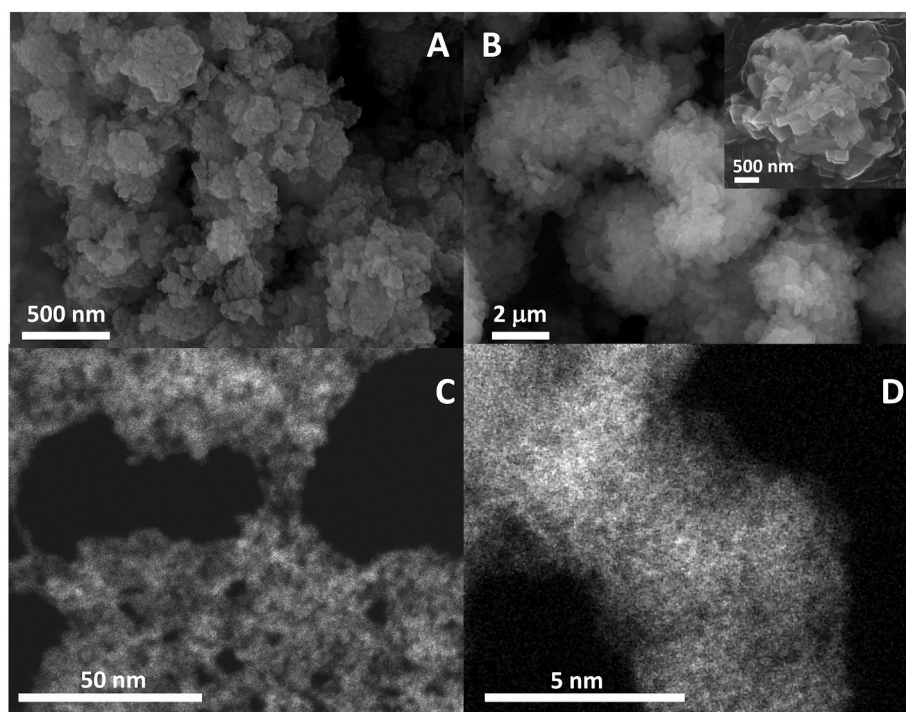


Fig. 1. SEM images of ZSM-5(40) (A) and ZSM-5(13) (B) zeolites and TEM images of embryonic zeolite (EZ) particles at low (C) and high (D) magnification. Inset B: close view of ZSM-13 aggregate.

Table 1

Framework composition, porosity, and concentration of Brønsted (B) and Lewis (L) acid sites determined by IR analysis of adsorbed pyridine (Py) of the studied samples.

Zeolite	Si/Al <sup>HCP</sup>	N <sub>2</sub> adsorption			Py adsorption			
		S <sub>BET</sub> /m <sup>2</sup> g <sup>-1</sup>	V <sub>mic</sub> /cm <sup>3</sup> g <sup>-1</sup>	V <sub>meso</sub> /cm <sup>3</sup> g <sup>-1</sup>	150 °C		250 °C	
					n(B)/μmol g <sup>-1</sup>	n(L)/μmol g <sup>-1</sup>	n(B)/μmol g <sup>-1</sup>	n(L)/μmol g <sup>-1</sup>
EZ	4.83	363	0.11	0.069	46	355	23	266
ZSM-5(40)	40	398	0.17	0.426	144	72	85	42
ZSM-5(13)	13	393	0.16	0.06	376	366	295	241
SiO <sub>2</sub> -Al <sub>2</sub> O <sub>3</sub>	3	55	0.01	0.157	10	104	–	–

Lewis acid sites. The chemically adsorbed pyridine exhibits a set of bands: two bands at 1545 and 1620 cm<sup>-1</sup> assigned to pyridinium ion (PyH<sup>+</sup>), and two bands at 1455, and 1620 cm<sup>-1</sup> related to coordinatively adsorbed pyridine on Lewis sites [44] (Fig. 3). The band at 1490 cm<sup>-1</sup> is attributed to Py species adsorbed on Lewis and Brønsted sites.

In agreement with the IR spectra of the OH groups, ZSM-5(40) has a moderate number of Brønsted sites and twice lower quantity of Lewis acid sites, while the ZSM-5(13) presents a rather high amount of both Brønsted and Lewis acid sites. The number of Brønsted sites in the EZ sample is lower than in the reference zeolite materials and comparable with the data previously reported on embryonic zeolites [12]. Further, the embryonic zeolite possesses a substantial amount of Lewis sites associated with the extra-framework Al. Amorphous aluminosilicate also has a low amount of Brønsted acid sites with a high contribution of Lewis acidity (Table 1). The strength of the acid sites has been compared by analysis of the desorption of Py with an increase of the temperature in the infrared cell (Fig. 3). Conventional ZSM-5(13) demonstrates a gradual decrease in the concentration of adsorbed Py with the increase of the temperature. Zeolite ZSM-5(40) presents a more significant decrease in the Py adsorption with the increase of the temperature. At the same time, in the embryonic zeolite, almost full desorption of Py is achieved already at 300 °C. These results indicate significantly lower strength of the acid sites in the embryonic zeolite in comparison with the commercial ZSM-5 reference materials. However, the strength of the

acid sites in the crystalline zeolites is significantly higher in comparison with amorphous aluminosilicate losing Py at already mild temperature. In order to understand the acidity difference between the crystalline and embryonic MFI zeolites, we performed DFT calculations.

### 3.2. DFT modeling

The crystalline MFI zeolites were simulated with two different Si/Al ratios of 47 and 3.8 (Figure S1, SI, MFI-47 and MFI-3.8), for which the acid strength was investigated by determining the pyridine adsorption energy ( $\Delta E_{\text{ads}}$ ). The Brønsted acid sites (BASs) located at the channel intersection were considered. The adsorption of pyridine leads to the proton transfer, which forms the protonated pyridine and the anionic zeolite framework (Fig. 4, MFI-47-py and MFI-3.8-py). The computed  $\Delta E_{\text{ads}}$  are -219 and -201 kJ/mol for the MFI-47 and MFI-3.8 zeolites, respectively, suggesting a higher acid strength of BAS in MFI-47 than in MFI-3.8. This trend indicates the acid strength increases with increasing Si/Al ratio, which is a widely reported phenomenon in zeolite chemistry [45–47]. The embryonic MFI was modeled by a defect model containing two BASs with partially eliminated surrounding framework atoms (Figure S1, SI MFI-defect). The adsorption of pyridine on the two BASs in the MFI-defect model affords the  $\Delta E_{\text{ads}}$  of -182 and -139 kJ/mol, respectively (Fig. 4, MFI-defect-site1-py and MFI-defect-site2-py), which signifies the lower acid strength of these sites in comparison with the

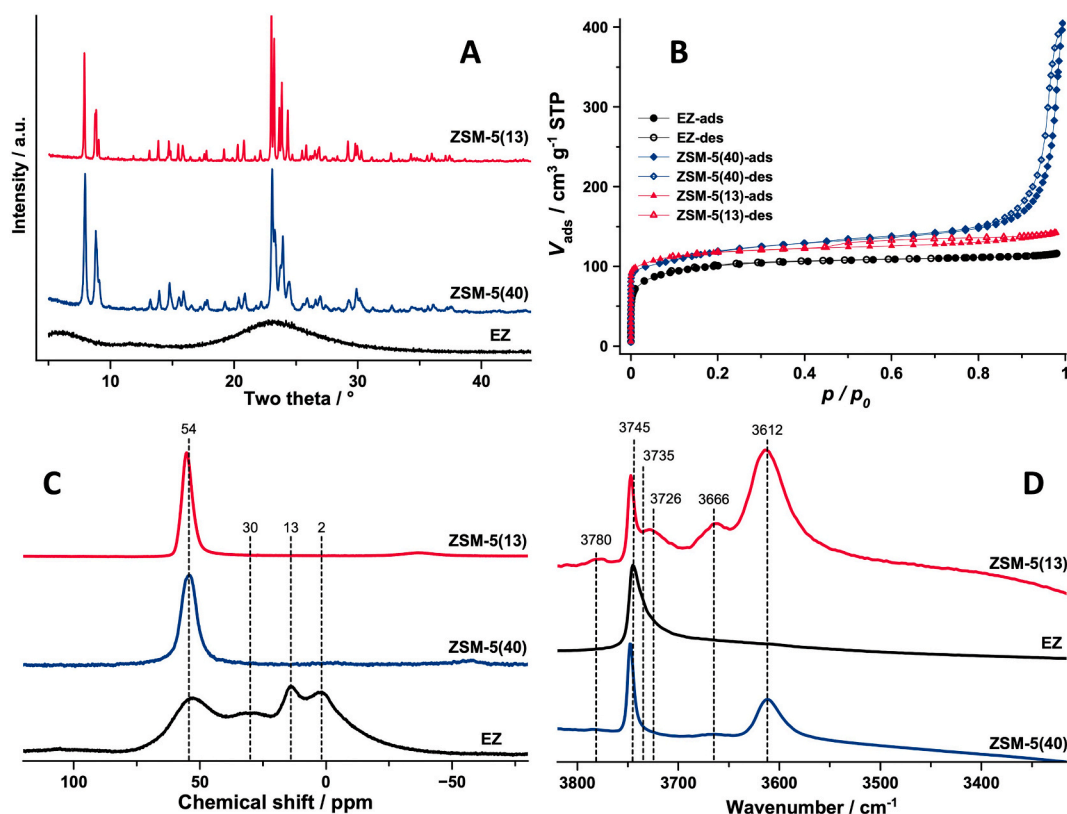


Fig. 2. Comparison of calcined ZSM-5(40) and ZSM-5(13) samples with the EZ zeolite: A) XRD patterns, B)  $N_2$  adsorption/desorption isotherms, C)  $^{27}Al$  MAS NMR spectra, D) FTIR spectra in the OH groups region.

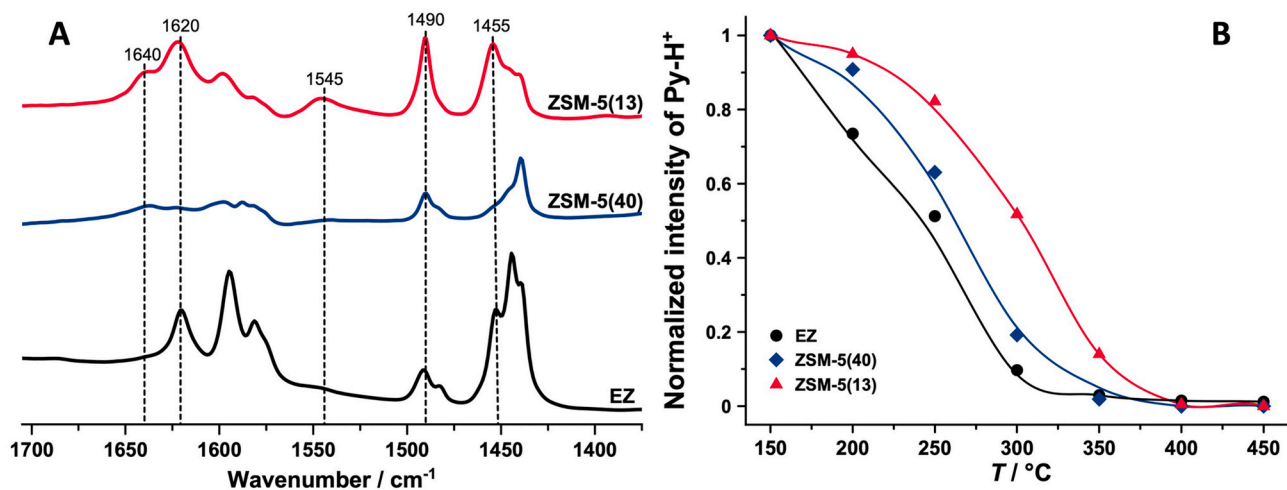


Fig. 3. Py adsorption over zeolites at 150 °C (A) and normalized amount of Py adsorbed over Brønsted acid sites versus temperature of Py desorption for ZSM-5 materials and EZ (B).

BASs in the crystalline MFI zeolites. In addition, the decrease in the acid strength is more significant when a larger portion of the framework atoms around the BASs was removed ( $-182$  vs.  $-139$  kJ/mol for MFI-defect-site1-py and MFI-defect-site2-py). This model matches well with the structure of EZ, where a substantial part of the unit cell is missing. The acidity trend for the crystalline and embryonic MFI suggests that the gradual formation of defect-free framework structures promotes a higher acid strength of the BASs in zeolites. The presented DFT results coincide with the experimental observation, which suggests the acid strength of the BASs is lower in the embryonic MFI than in the crystalline ones.

Lower acid strength in embryonic zeolites could be a direct consequence of the difference in the values of the Si-O-Al angles in comparison with crystalline zeolite. However, according to the results of the modeling there is no clear correlation between Si-O-Al angle and binding energy of Py (Table S2, SI). The strongest explanation for the weaker adsorption of pyridine on MFI-defect-site2 is the much lower dispersion contribution due to the less confined nature of the site. The “intrinsic” ( $E_{\text{elect}}$ ) binding energy after subtraction of dispersion contribution is quite similar for the low-silica model at Si/Al = 3.8 and the defect sites (Table S2, SI). Thus, a decrease in acidity could be explained by the changes in the local chemical composition of the zeolite (more silanols)

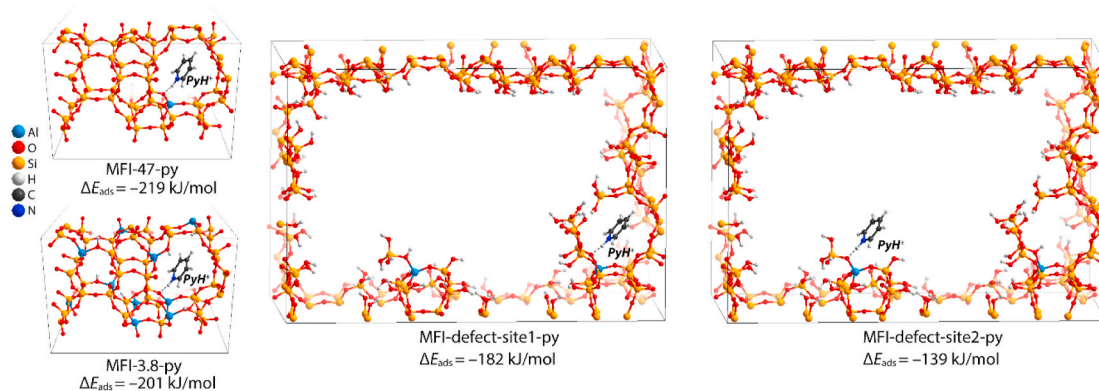


Fig. 4. Optimized structures of pyridine adsorption in the crystalline MFI zeolites with different Si/Al ratios [MFI-47-py (Si/Al = 47) and MFI-3.8-py (Si/Al = 3.8)] and the embryonic MFI zeolite represented by a defect model (Si/Al = 71) containing two BASs (MFI-defect-site1-py and defect-site2-py). The adsorption of pyridine on the BASs leads to the formation of protonated pyridine ( $\text{pyH}^+$ ) confined in zeolites. The acidity strength of the BASs was determined by the pyridine adsorption energy ( $\Delta E_{\text{ads}}$ ).

and the associated loss of crystallinity. The very strong decrease in the adsorption energy for the defect-site2 model is attributed to the most pronounced decrease of the dispersion stabilization of the adsorption complex due to the lack of the zeolite microenvironment near this site.

### 3.3. DME synthesis

The catalytic test of DME synthesis from syngas has been conducted over a mechanical mixture of CZA with embryonic zeolite and compared with the counterpart catalyst containing a crystalline zeolite and an amorphous aluminosilicate. The catalytic tests were performed at 260 °C and 20 bar at  $\text{H}_2/\text{CO}$  ratio 2. Dimethyl ether, methanol, carbon dioxide, hydrocarbons, and water were the major products of the reaction. We have conducted hydrogenation of CO over CZA catalyst at GHSV 3.6 L/g h (Fig. 5). The CZA catalyst has demonstrated the CO conversion of 17.8%, which is close to the thermodynamic equilibrium for hydrogenation of CO to methanol [48]. The main product of the reaction, in this case, is methanol (88.7%), with a small contribution of  $\text{CO}_2$  and DME. The lower yield of DME is due to the weak acidity of the catalyst.

Addition of the methanol dehydration function to the methanol synthesis catalysts should shift the thermodynamic equilibrium and favor DME formation by methanol dehydration over acid sites. It is noteworthy that the mechanical mixture of CZA with amorphous aluminosilicate does not exhibit higher activity compared to the CZA catalyst with the CO conversion close to 22%. However, some weak acidity of aluminosilicate induces an increase of the selectivity to DME

to 65%. Only very small amount of  $\text{CO}_2$  is produced. Fig. 5 displays the CO conversion for the mechanical mixtures of CZA with embryonic zeolite and commercial ZSM-5 zeolites. The conversion of CO in the presence of zeolites increases to 65–70%. Higher conversion is due to the enhanced rate of methanol dehydration to DME which shifts the equilibrium of the reaction. The activity increases in the row: ZSM-5(13) < ZSM-5(40) < EZ from 65 to 73.5%.

Methanol synthesis over the copper catalysts is a reversible reaction. At the reaction temperatures used in this work the yield of methanol from  $\text{H}_2/\text{CO}$  over a methanol synthesis catalyst depends on the thermodynamic equilibrium rather than reaction kinetics. The addition of the methanol dehydration function in the form of zeolite to the methanol synthesis catalyst shifts the thermodynamic equilibrium and favors DME formation. Thus, in bifunctional copper zeolite catalyst, the overall reaction rate will depend on the rates of methanol synthesis and dehydration reactions and transport phenomena which often strongly affect the reaction rate and selectivity in bifunctional catalysis [49]. The most important in this case should be the transport rate of methanol as intermediate from Cu catalyst to zeolite. It explains why the ultra-small embryonic zeolite with relatively weak acidity provides significantly higher activity for DME synthesis in comparison with large crystal ZSM-5 catalysts possessing stronger acidity. Indeed, the amount of acid sites decreases in the series ZSM-5(13) > ZSM-5(40) > EZ, opposite to the activity increase. The highest content of acid sites in ZSM-5(13) cannot compensate large size of zeolite crystals and diffusion limitations related to transfer of methanol from CZA to zeolite. The same effect

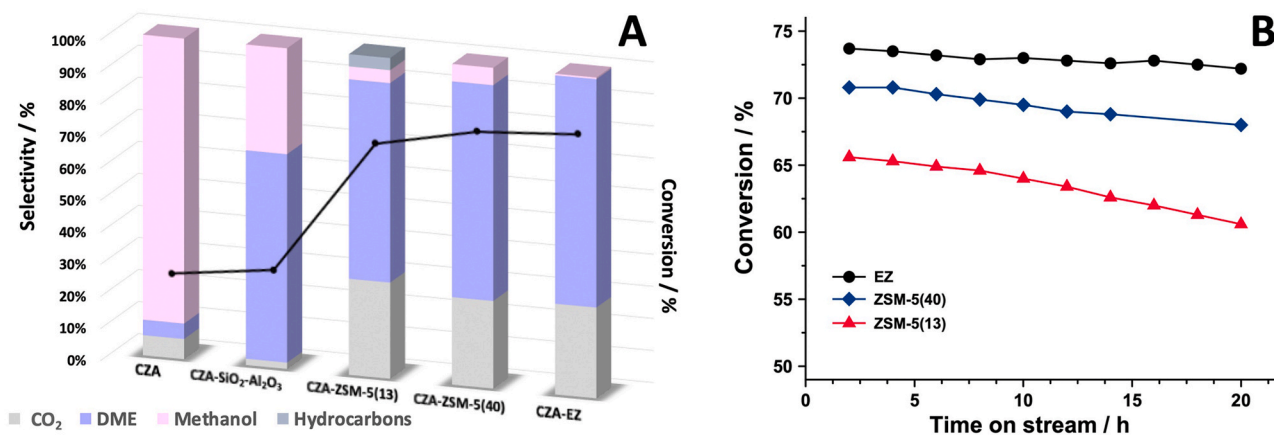


Fig. 5. Comparison of a mechanical mixture of ZSM-5, EZ, and aluminosilicate ( $\text{SiO}_2\text{-Al}_2\text{O}_3$ ) with CZA, and pure CZA: A) Carbon monoxide conversion and selectivity to the products ( $T = 260$  °C,  $P = 20$  bar,  $\text{H}_2/\text{CO} = 2$ , GHSV = 3.6 L/g h), and B) comparison of deactivation during DME synthesis from syngas over CZA/ZSM-5 and CZA/EZ ( $T = 260$  °C,  $P = 20$  bar,  $\text{H}_2/\text{CO} = 2$ , GHSV = 3.6 L/g h).

has been observed earlier using different size nanocrystals of ZSM-5 [28].

The high efficiency of embryonic zeolite in the catalytic performance of DME synthesis can be assigned to the enhanced transport of methanol produced on the CZA catalyst to the intimately mixed ultra-small embryonic zeolites. In this case, smaller, highly open zeolitic particles reduce methanol transport limitations and diffusion paths inside the pores. The methanol dehydration, in this case, occurs both inside the zeolite pores and on the external surface.

The selectivity to carbon dioxide is about 30% for the catalysts, which is close to the stoichiometric transformation of formed water during WGS from CO to CO<sub>2</sub>. Another product of syngas transformation over embryonic zeolite is DME, with selectivity close to 71% with only traces of other products. The selectivity to DME decreases in the row EZ > ZSM-5(40) > ZSM-5(13) with selectivity 64.6% for ZSM-5(13). The syngas transformation over ZSM-5(40) provides additionally to DME a significant amount of methanol (5.4%), which is the result of not full methanol dehydration to DME. In addition to the methanol, CZA-ZSM-5 (13) yields light hydrocarbons (ethylene, propylene ...) with selectivity 3.8%. The hydrocarbons presence indicates contribution of the MTO process [43] to the methanol conversion. This could be explained by the highest acidity of ZSM-5(13) zeolite in comparison with ZSM-5(40) and EZ. Consequently, the highest selectivity to DME over embryonic zeolite can be assigned to its mild acidity, besides the enhanced transport properties. According to pyridine adsorption and DFT modeling, embryonic zeolite possesses milder acidity induced by a defected structure, which provides efficient dehydration of methanol to DME without a deeper transformation toward hydrocarbons.

Fig. 5B displays CO conversion measured on the catalysts as a function of reaction time. Carbon monoxide conversion decreases over ZSM-5(13) from 65.6 to 60.6% for 20 h with time on stream, which can be attributed to the catalyst deactivation. ZSM-5(40) provides better stability during DME synthesis, with a decrease of the CO conversion from 70.8 to 68%. It is worth noting that the embryonic zeolite provides much higher stability, with only a slight catalyst deactivation in time. Previous reports suggest that the deactivation of CZA@ZSM-5 catalysts can be due to several phenomena: copper sintering, copper oxidation, and migration to the cationic positions of zeolite, coke deposition [29, 30, 50, 51]. All these effects are induced by the strong acid sites interacting with copper or generating coke species. Earlier, we have identified that zeolite external acidity is a particularly important factor in catalyst deactivation due to close contact with the CZA catalyst [30]. The fast deactivation rate of ZSM-5(13) containing catalyst can be explained by zeolite's strong acidity, leading to interaction and oxidation of Cu. Moderate acidity of embryonic zeolites attenuates the negative effects related to copper oxidation, migration and coke formation. Moreover, the embryonic zeolites with their cage-like structure of a few nano-meter sizes do not exhibit strong external acidity in terms of crystalline zeolite-type material. Thus, these materials are particularly appropriate for preparing a hybrid catalyst for DME synthesis from syngas.

To conclude, our results show significantly higher activity, selectivity, and stability toward DME synthesis over the hybrid catalyst containing embryonic zeolite in comparison with crystalline ZSM-5. The mild acidity and small size of embryonic zeolite nanoparticles mixed with Cu catalyst provide efficient and stable dehydration of intermediate methanol to DME.

#### 4. Conclusion

The obtained results pinpoint the excellent performance of the embryonic zeolite-CuO-ZnO-Al<sub>2</sub>O<sub>3</sub> hybrid catalyst for direct DME synthesis. The EZ-containing catalyst demonstrates high activity, selectivity, and stability compared to the conventional ZSM-5 zeolite and amorphous aluminosilicate counterparts. The set of experimental data revealed that the superior catalytic performance is due to two key

features of embryonic zeolite:

- ✓ ultra-small nanoparticles (<5 nm)
- ✓ medium strength of Brønsted acid sites.

Ultra-small nanoparticles of embryonic zeolite exhibit reduced diffusion paths and thus diminish the transport limitation. Further, the small size facilitates intimate mixing with the Cu-Zn-Al phase. In this way is achieved enhanced methanol transport phenomena from the copper catalyst to the acid sites in bi-functional hybrid catalysts. This results in higher activity of the embryonic zeolite-based catalysts. The strength of the acid sites in embryonic zeolite lies in between the strong acid sites in fully-crystalline zeolite and the weak ones in amorphous aluminosilicate. The DFT modeling supports the experimental data and confirms the decrease in the acid strength due to the loss of structure ordering in the embryonic zeolite. The medium strength of the acid sites contributes to the significantly higher selectivity to DME and the high stability of the catalyst. Indeed, the results obtained in the scope of this study designate a new avenue for tailoring of hybrid and bifunctional catalysts.

#### CRediT authorship contribution statement

**Ana Palčić:** Conceptualization, Methodology, Experiments, Draft preparation. **Sara Navarro Jaén:** Catalytic experiments. **Dan Wu:** Catalytic experiments. **Mengdie Cai:** Catalytic experiments. **Chong Liu:** DFT modelling. **Evgeny A. Pidko:** Methodology of DFT modelling. **Andrei Y. Khodakov:** Design of Experiments, Discussion, Writing, Editing. **Vitaly Ordonsky:** Supervision, Design of Experiments, Discussion, Writing, Editing. **Valentin Valtchev:** Supervision, Design of Experiments, Discussion, Writing, Editing.

#### Declaration of competing interest

The authors declare that they have no known competing financial interests or personal relationships that could have appeared to influence the work reported in this paper.

#### Acknowledgements

V.O. acknowledges the financial support of the French National Research Agency (NANO4-FUT, Ref. ANR-16-CE06-0013). V.V. acknowledges the support from the ANR-TOTAL Industrial Chair "Nanoclean Energy" (Ref. ANR-17-CHIN-0005-01). S.N.J and A.Y.K acknowledge the support from "Electrons to high value Chemical products" (E2C 2 Seas Interreg project). The use of the national computer facilities for DFT calculations was subsidized by NWO Domain Science.

#### Appendix A. Supplementary data

Supplementary data to this article can be found online at <https://doi.org/10.1016/j.micromeso.2021.111138>.

#### References

- [1] J. Pérez-Ramírez, C.H. Christensen, K. Egeblad, C.H. Christensen, J.C. Groen, Hierarchical zeolites: enhanced utilisation of microporous crystals in catalysis by advances in materials design, *Chem. Soc. Rev.* 37 (11) (2008) 2530–2542.
- [2] E.M. Gallego, C. Li, C. Paris, N. Martín, J. Martínez-Triguero, M. Boronat, M. Moliner, A. Corma, Making nanosized CHA zeolites with Controlled Al Distribution for Optimizing methanol-to-olefin performance, *Chem. Eur. J.* 24 (55) (2018) 14631–14635.
- [3] Q. Zhang, S. Xiang, Q. Zhang, B. Wang, A. Mayoral, W. Liu, Y. Wang, Y. Liu, J. Shi, G. Yang, J. Luo, X. Chen, O. Terasaki, J.-P. Gilson, J. Yu, Breaking the Si/Al limit of nanosized  $\beta$  zeolites: promoting catalytic production of lactide, *Chem. Mater.* 32 (2) (2020) 751–758.
- [4] H. Awala, J.P. Gilson, R. Retoux, P. Boullay, J.M. Goupil, V. Valtchev, S. Mintova, Template-free nanosized faujasite-type zeolites, *Nat. Mater.* 14 (4) (2015) 447–451.

- [5] C. Peng, Z. Liu, Y. Yonezawa, N. Linares, Y. Yanaba, C.A. Trujillo, T. Okubo, T. Matsumoto, J. García-Martínez, T. Wakihara, Testing the limits of zeolite structural flexibility: ultrafast introduction of mesoporosity in zeolites, *J. Mater. Chem.* 8 (2) (2020) 735–742.
- [6] V. Valtchev, E. Balanzat, V. Mavrodinova, I. Diaz, J. El Fallah, J.-M. Goupil, High energy ion irradiation-induced ordered macropores in zeolite crystals, *J. Am. Chem. Soc.* 133 (46) (2011) 18950–18956.
- [7] H. Hernando, A.M. Hernández-Giménez, C. Ochoa-Hernández, P.C.A. Bruijninx, K. Houben, M. Baldus, P. Pizarro, J.M. Coronado, J. Feroso, J. Čejka, B. M. Weckhuysen, D.P. Serrano, Engineering the acidity and accessibility of the zeolite ZSM-5 for efficient bio-oil upgrading in catalytic pyrolysis of lignocellulose, *Green Chem.* 20 (15) (2018) 3499–3511.
- [8] R.F. Lobo, M. Tsapatsis, C.C. Freyhardt, S. Khodabandeh, P. Wagner, C.-Y. Chen, K. J. Balkus, S.I. Zones, M.E. Davis, Characterization of the extra-large-pore zeolite UTD-1, *J. Am. Chem. Soc.* 119 (36) (1997) 8474–8484.
- [9] K.-G. Haw, J.-M. G., J.-P. Gilson, N. Nesterenko, D. Minoux, J.-P. Dath, Catalyst Compositions Comprising Ultra-small Size Molecular Sieves Crystals Deposited on a Porous Material, WO2015001004, 2015.
- [10] K.-G. Haw, J.-M. Goupil, J.-P. Gilson, N. Nesterenko, D. Minoux, J.-P. Dath, V. Valtchev, Embryonic ZSM-5 zeolites: zeolitic materials with superior catalytic activity in 1,3,5-triisopropylbenzene dealkylation, *New J. Chem.* 40 (5) (2016) 4307–4313.
- [11] K.-G. Haw, J.-P. Gilson, N. Nesterenko, M. Akouche, H. El Siblani, J.-M. Goupil, B. Rigaud, D. Minoux, J.-P. Dath, V. Valtchev, Supported embryonic zeolites and their use to process bulky molecules, *ACS Catal.* 8 (9) (2018) 8199–8212.
- [12] M. Akouche, J.-P. Gilson, N. Nesterenko, S. Moldovan, D. Chateigner, H.E. Siblani, D. Minoux, J.-P. Dath, V. Valtchev, Synthesis of embryonic zeolites with controlled physicochemical properties, *Chem. Mater.* 32 (5) (2020) 2123–2132.
- [13] T.A. Semelsberger, R.L. Borup, H.L. Greene, Dimethyl ether (DME) as an alternative fuel, *J. Power Sources* 156 (2) (2006) 497–511.
- [14] Z. Azizi, M. Rezaeiamesh, T. Tohidian, M.R. Rahimpour, Dimethyl ether: a review of technologies and production challenges, *Chem. Eng. Process: Process Intensification* 82 (2014) 150–172.
- [15] H.-J. Chen, C.-W. Fan, C.-S. Yu, Analysis, synthesis, and design of a one-step dimethyl ether production via a thermodynamic approach, *Appl. Energy* 101 (2013) 449–456.
- [16] Y. Wang, Y. Chen, F. Yu, D. Pan, B. Fan, J. Ma, R. Li, One-step synthesis of dimethyl ether from syngas on ordered mesoporous copper incorporated alumina, *Journal of Energy Chemistry* 25 (5) (2016) 775–781.
- [17] J.W. Jung, Y.J. Lee, S.H. Um, P.J. Yoo, D.H. Lee, K.-W. Jun, J.W. Bae, Effect of copper surface area and acidic sites to intrinsic catalytic activity for dimethyl ether synthesis from biomass-derived syngas, *Appl. Catal. B Environ.* 126 (2012) 1–8.
- [18] G. Yang, N. Tsubaki, J. Shamoto, Y. Yoneyama, Y. Zhang, Confinement effect and synergistic function of H-ZSM-5/Cu-ZnO-Al<sub>2</sub>O<sub>3</sub> capsule catalyst for one-step controlled synthesis, *J. Am. Chem. Soc.* 132 (23) (2010) 8129–8136.
- [19] G.C. Chinchin, K.C. Waugh, D.A. Whan, The activity and state of the copper surface in methanol synthesis catalysts, *Appl. Catal.* 25 (1) (1986) 101–107.
- [20] P.L. Hansen, J.B. Wagner, S. Helveg, J.R. Rostrup-Nielsen, B.S. Clausen, H. Topsøe, Atom-resolved imaging of dynamic shape changes in supported copper nanocrystals 295 (5562) (2002) 2053–2055.
- [21] J.B. Wagner, P.L. Hansen, A.M. Molenbroek, H. Topsøe, B.S. Clausen, S. Helveg, In situ electron energy loss spectroscopy studies of gas-dependent Metal–Support interactions in Cu/ZnO catalysts, *J. Phys. Chem. B* 107 (31) (2003) 7753–7758.
- [22] Y. Okamoto, K. Fukino, T. Imanaka, S. Teranishi, Surface characterization of copper(II) oxide-zinc oxide methanol-synthesis catalysts by x-ray photoelectron spectroscopy. 2. Reduced catalysts, *J. Phys. Chem.* 87 (19) (1983) 3747–3754.
- [23] V. Vishwanathan, K.-W. Jun, J.-W. Kim, H.-S. Roh, Vapour phase dehydration of crude methanol to dimethyl ether over Na-modified H-ZSM-5 catalysts, *Appl. Catal. Gen.* 276 (1) (2004) 251–255.
- [24] J. Fei, Z. Hou, B. Zhu, H. Lou, X. Zheng, Synthesis of dimethyl ether (DME) on modified HY zeolite and modified HY zeolite-supported Cu–Mn–Zn catalysts, *Appl. Catal. Gen.* 304 (2006) 49–54.
- [25] J.-H. Kim, M.J. Park, S.J. Kim, O.-S. Joo, K.-D. Jung, DME synthesis from synthesis gas on the admixed catalysts of Cu/ZnO/Al<sub>2</sub>O<sub>3</sub> and ZSM-5, *Appl. Catal. Gen.* 264 (1) (2004) 37–41.
- [26] J.W. Bae, S.-H. Kang, Y.-J. Lee, K.-W. Jun, Synthesis of DME from syngas on the bifunctional Cu–ZnO–Al<sub>2</sub>O<sub>3</sub>/Zr-modified ferrierite: effect of Zr content, *Appl. Catal. B Environ.* 90 (3) (2009) 426–435.
- [27] A. García-Trenco, S. Valencia, A. Martínez, The impact of zeolite pore structure on the catalytic behavior of CuZnAl/zeolite hybrid catalysts for the direct DME synthesis, *Appl. Catal. Gen.* 468 (2013) 102–111.
- [28] M. Cai, A. Palčić, V. Subramanian, S. Moldovan, O. Ersen, V. Valtchev, V. Ordonsky, A.Y. Khodakov, Direct dimethyl ether synthesis from syngas on copper–zeolite hybrid catalysts with a wide range of zeolite particle sizes, *J. Catal.* 338 (2016) 227–238.
- [29] F.S.R. Barbosa, V.S.O. Ruiz, J.L.F. Monteiro, R.R. de Avillez, L.E.P. Borges, L. G. Appel, The deactivation modes of Cu/ZnO/Al<sub>2</sub>O<sub>3</sub> and HZSM-5 physical mixture in the one-step DME synthesis, *Catal. Lett.* 126 (1) (2008) 173–178.
- [30] V.V. Ordonsky, M. Cai, V. Sushkevich, S. Moldovan, O. Ersen, C. Lancelot, V. Valtchev, A.Y. Khodakov, The role of external acid sites of ZSM-5 in deactivation of hybrid CuZnAl/ZSM-5 catalyst for direct dimethyl ether synthesis from syngas, *Appl. Catal. Gen.* 486 (2014) 266–275.
- [31] I. Sierra, J. Erena, J.M. Arandes, M. Olazar, J. Bilbao, Aguayo, A. T., Co-feeding water to attenuate deactivation of the catalyst metallic function (CuO–ZnO–Al<sub>2</sub>O<sub>3</sub>) by coke in the direct synthesis of dimethyl ether, *Appl. Catal. B Environ.* 106 (1) (2011) 167–173.
- [32] C.A. Emeis, Determination of integrated molar extinction coefficients for infrared absorption bands of pyridine adsorbed on solid acid catalysts, *J. Catal.* 141 (2) (1993) 347–354.
- [33] G. Kresse, J. Hafner, Ab initio molecular dynamics for open-shell transition metals, *Phys. Rev. B* 48 (17) (1993) 13115–13118.
- [34] G. Kresse, J. Hafner, Ab initio molecular-dynamics simulation of the liquid-metal–amorphous-semiconductor transition in germanium, *Phys. Rev. B* 49 (20) (1994) 14251–14269.
- [35] G. Kresse, J. Furthmüller, Efficient iterative schemes for ab initio total-energy calculations using a plane-wave basis set, *Phys. Rev. B* 54 (16) (1996) 11169–11186.
- [36] J.P. Perdew, K. Burke, M. Ernzerhof, Generalized gradient approximation made simple, *Phys. Rev. Lett.* 77 (18) (1996) 3865–3868.
- [37] P.E. Blöchl, Projector augmented-wave method, *Phys. Rev. B* 50 (24) (1994) 17953–17979.
- [38] G. Kresse, D. Joubert, From ultrasoft pseudopotentials to the projector augmented-wave method, *Phys. Rev. B* 59 (3) (1999) 1758–1775.
- [39] J.D. Pack, H.J. Monkhorst, Special points for Brillouin-zone integrations—a reply, *Phys. Rev. B* 16 (4) (1977) 1748–1749.
- [40] S. Grimme, S. Ehrlich, L. Goerigk, Effect of the damping function in dispersion corrected density functional theory 32 (7) (2011) 1456–1465.
- [41] D.H. Olson, G.T. Kokotailo, S.L. Lawton, W.M. Meier, Crystal structure and structure-related properties of ZSM-5, *J. Phys. Chem.* 85 (15) (1981) 2238–2243.
- [42] T. Matthias, K. Katsumi, V.N. Alexander, P.O. James, R.-R. Francisco, R. Jean, S.W. S. Kenneth, Physisorption of gases, with special reference to the evaluation of surface area and pore size distribution (IUPAC Technical Report), *Pure Appl. Chem.* 87 (9–10) (2015) 1051–1069.
- [43] A. Palčić, V.V. Ordonsky, Z. Qin, V. Georgieva, V. Valtchev, Tuning zeolite properties for a highly efficient synthesis of propylene from methanol 24 (50) (2018) 13136–13149.
- [44] G. Crépeau, V. Montouillout, A. Vimont, L. Maréy, T. Cseri, F. Maugé, Nature, structure and strength of the acidic sites of amorphous silica Alumina: an IR and NMR study, *J. Phys. Chem. B* 110 (31) (2006) 15172–15185.
- [45] A. Primo, H. Garcia, Zeolites as catalysts in oil refining, *Chem. Soc. Rev.* 43 (22) (2014) 7548–7561.
- [46] J. Dwyer, F.R. Fitch, E.E. Nkang, Dependence of zeolite properties on composition. Unifying concepts, *J. Phys. Chem.* 87 (26) (1983) 5402–5404.
- [47] C. Liu, G. Li, E.J.M. Hensen, E.A. Pidko, Relationship between acidity and catalytic reactivity of faujasite zeolite: a periodic DFT study, *J. Catal.* 344 (2016) 570–577.
- [48] W.-J. Shen, K.-W. Jun, H.-S. Choi, K.-W. Lee, Thermodynamic investigation of methanol and dimethyl ether synthesis from CO<sub>2</sub> Hydrogenation, *Kor. J. Chem. Eng.* 17 (2) (2000) 210–216.
- [49] P.B. Weisz, Polyfunctional heterogeneous catalysis, in: D.D. Eley, P.W. Selwood, P. B. Weisz, A.A. Balandin, J.H. De Boer, P.J. Debye, P.H. Emmett, J. Horvut, W. Jost, G. Natta, E.K. Rideal, H.S. Taylor (Eds.), *Advances in Catalysis*, vol. 13, Academic Press, 1962, pp. 137–190.
- [50] R. Montesano, A. Narvaez, D. Chadwick, Shape-selectivity effects in syngas-to-dimethyl ether conversion over Cu/ZnO/Al<sub>2</sub>O<sub>3</sub> and zeolite mixtures: carbon deposition and by-product formation, *Appl. Catal. Gen.* 482 (2014) 69–77.
- [51] A. Ciftci, D. Varisli, K. Cem Tokay, N. Aslı Sezgi, T. Dogu, Dimethyl ether, diethyl ether & ethylene from alcohols over tungstophosphoric acid based mesoporous catalysts, *Chem. Eng. J.* 207–208 (2012) 85–93.